Neuroinvasive potential of SARS-CoV-2 revealed in a human brain organoid model

Eric Song[1*], Ce Zhang[2,3*], Benjamin Israelow[1,4], Peiwen Lu[1], Orr-El Weizman[1], Feimei Liu[1,5], Yile Dai[1], Klara Szigeti-Buck[3,6], Yuki Yasumoto[3,6], Guilin Wang[7], Christopher Castaldi[7], Jaime Heltke[7], Evelyn Ng[7], John Wheeler[7], Mia Madel Alfajaro[1,8], Benjamin Fontes[9], Neal G. Ravindra[10,11], David Van Dijk[10,11], Shrikant Mane[2,7], Murat Gunel[2,3,12], Aaron Ring[1], Craig B Wilen[1,8], Tamas L. Horvath[6,13,14], Angeliki Louvi[3,12], Shelli F. Farhadian[4,15], Kaya Bilguvar[2,7,#], Akiko Iwasaki[1,14,16,#]

[1] Department of Immunobiology, Yale School of Medicine, New Haven, CT, USA
[2] Department of Genetics, Yale School of Medicine, New Haven, CT, USA
[3] Department of Neuroscience, Yale School of Medicine, New Haven, CT, USA
[4] Department of Internal Medicine, Section of Infectious Diseases, Yale School of Medicine, New Haven, CT, USA
[5] Department of Biomedical Engineering, Yale University, New Haven, CT, USA
[6] Department of Comparative Medicine, Yale School of Medicine, New Haven, CT, USA
[7] Yale Center for Genome Analysis, West Haven, CT, USA
[8] Department of Laboratory Medicine, Yale School of Medicine, New Haven, CT, USA.
[9] Yale Environmental Health and Safety, Yale University, New Haven, CT, USA
[10] Cardiovascular Research Center, Section of Cardiovascular Medicine, Department of Internal Medicine, Yale School of Medicine, New Haven, CT, USA
[11] Department of Computer Science, Yale University, New Haven, CT, USA
[12] Department of Neurosurgery, Yale School of Medicine, New Haven, CT, USA
[13] Department of Molecular Biophysics and Biochemistry, Yale School of Medicine, New Haven, CT, USA
[14] Department of Molecular, Cellular, and Developmental Biology, Yale School of Medicine, New Haven, CT, USA
[15] Department of Neurology, Yale School of Medicine, New Haven, CT, USA
[16] Howard Hughes Medical Institute, Chevy Chase, MD, USA
[*]These Authors contributed equally to this work
[#]Corresponding Authors

Abstract

Although COVID-19 is considered to be primarily a respiratory disease, SARS-CoV-2 affects multiple organ systems including the central nervous system (CNS). Reports indicate that 30-60% of patients with COVID-19 suffer from CNS symptoms. Yet, there is no consensus whether the virus can infect the brain, or what the consequences of infection are. Following SARS-CoV-2 infection of human brain organoids, clear evidence of infection was observed, with accompanying metabolic changes in the infected and neighboring neurons. Further, no evidence for the type I interferon responses was detected. We demonstrate that neuronal infection can be prevented either by blocking ACE2 with antibodies or by administering

cerebrospinal fluid from a COVID-19 patient. Finally, using mice overexpressing human ACE2, we demonstrate *in vivo* that SARS-CoV-2 neuroinvasion, but not respiratory infection, is associated with mortality. These results provide evidence for the neuroinvasive capacity of SARS-CoV2, and an unexpected consequence of direct infection of neurons by SARS-CoV2.

As of June 2020, SARS-CoV-2 has infected over seven million people globally. While a majority of COVID-19 patients present with respiratory symptoms, neurological involvement, including impaired consciousness and headache, have been reported in patients (*1*). To date, human autopsy studies have identified viral RNA transcripts (*2, 3*) along with viral proteins (*4*) in brain tissues of a small proportion of people who succumbed to COVID-19. However, the replicative potential of SARS-CoV-2 in neural tissues remain undefined.

To dissect the mode and consequences of infection, we first established the neuroinvasive potential of SARS-CoV-2 in a human brain model system. We first utilized human induced pluripotent stem cell (hiPSC) lines (Y1 and Y6), derived from healthy individuals (fig. S1), to generate forebrain-specific human neural progenitor cells (hNPCs). In culture, we observed replication of SARS-CoV-2 in two-week-old hNPCs, with peak viral titers as early as 12 h post infection (hpi) (fig. S2A and B). In addition, TUNEL staining indicated increased cell death (fig. S2A). Next, we generated hiPSC-derived brain organoids (*5-8*) to model the SARS-CoV-2 infection of neuronal cells in 3D. Similar to a recent report (*9*), we observed infection of neuronal cells in nine-week-old organoids as early as 24 hpi, with significantly increased number of SARS-CoV-2 positive cells at 96 hpi (Fig. 1A-C, fig. S2C). Although the majority of the SARS-CoV-2 infected cells were localized within MAP2 positive cellular fields of mature neurons (Fig. 1B.2, fig. S2C), we also observed infection of SOX2-positive neural stem cells with bipolar morphology and cells localized around the neural tube-like structures (Fig. 1B.1). We observed an increase in SARS-CoV-2 positive cells 96 hpi compared to 24 hpi (Fig. 1C, fig. S2C-E). Using electron microscopy, we visualized viral particles within the organoid (Fig. 1D, fig. S3), with discrete regions of high-density virus accumulation (Fig. 1D.1) and other regions showing viral budding from endoplasmic reticulum-like structures (Fig. 1D.2-4), suggesting SARS-CoV-2 is able to utilize the neuronal cell machinery to replicate. Organoid infection resulted in extensive neuronal cell death; strikingly, however, the majority of TUNEL-positive cells were SARS-CoV-2 negative (Fig. 1E and F), and only ~15% of the cells infected with SARS-CoV-2 were TUNEL-positive (Fig. 1G). Increased cell death was correlated with a higher density of SARS-CoV-2 positive cells (Fig. 1H), which however, were not overtly dying (Fig. 1F and G). Even within a single plane, we noticed high density SARS-CoV-2 area to have more TUNEL-positive cells (Fig. 1I yellow box) compared to low-density SARS-CoV-2 regions (Fig. 1I white box). Together, these data suggested that SARS-CoV-2 can infect cells of neural origin, and infected cells can promote death of nearby cells.

We hypothesized that the cellular heterogeneity of brain organoids may be leading to certain cells being more susceptible to infection and others to death and that this system would

provide an ideal platform to understand the cellular tropism of SARS-CoV-2 in the CNS and elucidate the consequences of SARS-CoV-2 neuroinvasion. To address these questions, we performed single-cell RNA sequencing to dissect the cellular states and transcriptional changes occurring after SARS-CoV-2 infection in both infected and non-infected cells within the organoid. We analyzed 60-day-old organoids that were either mock infected or infected with SARS-CoV-2 and collected at 2, 24, and 96 hpi (n = 2 for each time point); 96,205 cells were used to create 31 distinct clusters (fig. S4A). Annotations from previous studies (*8, 10, 11*) allowed us to characterize the identity of each cluster (fig. S4C). Monocle trajectory further classified these clusters into four major cellular states (Fig. 2A, fig. S4B); Neural progenitors/outer radial glia, intermediate progenitor/interneurons, neurons, and cortical neurons (Fig. 2B). Comparing global UMAP clusters in specimens collected before and after infection, we were able to identify cellular population changes during infection (fig. S4D and S5). With an added SARS-CoV-2 annotation, SARS-CoV-2 transcript reads were localized to a variety of cell clusters (Fig. 2C and fig. S4E), demonstrating the widespread infectivity of SARS-CoV-2 in neurons, radial glia and neuronal progenitor cells. Several cell clusters—defined in Fig. S4—showed large changes in their representation within the organoid, such as cluster 1 (from 5% to roughly 20% of the population), or cluster 7 (from ~10% to nearly 0%) (Fig. 2D). However, this was not uniformly seen with all infected clusters, as cells in cluster 11 showed high infection rates (Fig. 2C), but with little change in population representation (Fig. 2D, fig. S4F). This is consistent with findings from TUNEL staining (Fig. 1E-G), which demonstrated minimal overlap between SARS-CoV-2 infected cells and those undergoing cell death.

To investigate the underlying molecular mechanisms, we compared the changes in the transcriptome of SARS-CoV-2 infected organoids with another well-studied neurotropic virus—Zika virus (ZIKV). Differentially expressed genes (DEGs) after a brain organoid infection with ZIKV (*12*) showed almost no overlap with DEGs from SARS-CoV-2 infected organoids (Fig. 2E). In both cases the transcriptome showed evidence of viral infection and invasion (Fig. 2F). However, unique processes were enriched in each of the infections. SARS-CoV-2 infected brain organoid upregulated pathways related to cell division, organelle fission and metabolic processes, while ZIKV showed enrichment in type I interferon pathways (Fig. 2F). SARS-Cov-2 induced a unique transcriptional state within neurons compared to ZIKV —consistent with the fact that SARS-CoV-2 induces a moderate interferon-stimulate gene (ISG) response in other tissues (*13*), and previous reports of specific virus replication being controlled by alternative pathways by neurons (*14, 15*).

To understand the impact of SARS-CoV-2 infection on the brain organoid at the cellular level, we characterized cells that were infected with SARS-CoV-2 versus neighboring uninfected cells without the presence of SARS-CoV-2 transcript, in a cluster comprising the highest number of infected cells at 96 hpi. SARS-CoV-2-positive cells showed enrichment of genes corresponding to viral transcription, along with enrichment for metabolic processes including electron transport coupled proton transport, cytochrome c to oxygen, and NADH to ubiquinone (Fig. 2G top panel). Conversely, SARS-CoV-2-negative cells showed a mitochondrial catabolic state with the upregulation of alcohol metabolism, cholesterol synthesis, and regulation of cell death (Fig. 2G bottom panel). These two cell populations displayed antagonizing pathway enrichment, with the infected cells responding to hyperoxia and the bystander cells responding to hypoxia (Fig. 2G highlight in yellow). The hypermetabolic state is unique to the SARS-CoV-2 infected cells (Fig. 2H) and highlights the ability of SARS-CoV-2 to hijack the host neuron machinery to replicate (Fig. 1D). Finally, we confirmed that infection by SARS-CoV-2 induced a locally hypoxic environment in neuronal regions by staining for HIF1α (Figure 2I and J) in mock infected and SARS-CoV-2 infected organoids. Together these results indicate the potential of SARS-CoV-2 in manipulating host metabolic programming that may create a resource-restricted environment for cells.

The question remains whether or not ACE2 is the main route of entry of SARS-CoV-2 into neuronal cells and what strategies might block viral infection. ACE2 expression in the CNS, and in neurons in particular, is still unclear (*16*). Moreover, in addition to ACE2, other cofactors such as TMPRSS2 (*17*) and Neuropilin-1 (*4, 18*) seem to affect infection rates. One of the main arguments against SARS-CoV-2 neuroinvasion lies in the fact that the mRNA levels of ACE2 appear to be very low in the CNS (*19-21*). Indeed, our single cell RNA-seq data set demonstrated low levels of ACE2; it was, however, detectable in many clusters (fig. S6A). In addition, we did not observe a correlation between the percentage of cells infected in each cluster to either ACE2, TMPRSS2 or Neuropilin-1 expression (fig. S6B). However, it remained possible that ACE2 protein may be expressed on the cell surface to promote viral entry. Consistent with this idea, we found widespread expression of ACE2 protein in both MAP2-positive neurons and cells close to the lumen of the organoids (Fig. 3A), indicating that the mRNA level of ACE2 is not the best surrogate for ACE2 protein expression. To test the requirement of ACE2 for SARS-CoV-2 infection, we incubated organoids with an anti-ACE2 blocking monoclonal antibody prior to infection with SARS-CoV-2. We detected significant inhibition of SARS-CoV-2 infection upon pre-treatment with ACE2 antibody compared with

isotype control, indicating the requirement of ACE2 for infection of brain organoids (Fig. 3B and 3F, fig. S6C).

Next, we investigated whether there are humoral antibody responses against SARS-CoV-2 in the CNS of infected patients, and whether antibodies present in the CNS can prevent infection of neurons. We analyzed cerebrospinal fluid (CSF) from a patient hospitalized with COVID-19 and acute encephalopathy (Fig. 3C) and from a healthy control volunteer by performing ELISA against the spike protein of SARS-CoV-2 (Fig. 3D). We detected IgG antibodies specific to the spike protein in the patient CSF even at 100x dilutions (Fig. 3D). Using this patient's CSF, we performed a neutralization assay against SARS-CoV-2 and validated its efficacy in preventing brain organoid infection (Fig. 3E). CSF-containing antiviral antibodies blocked SARS-CoV-2 infection in organoids (Fig. 3E and F, fig. S6D), highlighting the potential of SARS-CoV-2 neuroinvasion and subsequent immune response in the CNS.

Finally, we examined the neuroinvasive potential of SARS-CoV-2 and the consequences of infection in vivo by using transgenic mice expressing human ACE2 under the K18 promoter (K18-hACE2) (*22*). Similar to previous reports of SARS-CoV showing neurotropism (*22, 23*), we observed increasing viral titers in the brain of mice after intranasal administration of SARS-CoV-2 (Fig. 4A and B). Immunofluorescent images showed wide distribution of SARS-CoV-2. At day 4 post infection (DPI) we observed perinuclear SARS-CoV-2 staining that did not colocalize with either astroglia (GFAP) or microglia (IBA1) markers. However, by 7 DPI, most of the SARS-CoV-2 staining localized with IBA1 positive cells, which cells adopted an increasingly amoeboid shape compared to the ramified shape of uninfected cells, indicating microglia activation (Fig. 4C). Similar to SARS-CoV (*23*), we did not detect overt astrogliosis following infection with SARS-CoV-2 (Fig. 4B).

To dissect the consequences of SARS-CoV-2 infection in the CNS versus the respiratory system, we directed expression of human ACE2 using an adeno-associated virus vector (AAV-hACE2) (*24*) to the lungs via intratracheal (IT) delivery or to the brain via intracisternal (IC) delivery (Fig. 4D). Then, the mice were infected with SARS-CoV-2 respectively, either intranasally or intraventricularly. Intranasally infected mice showed signs of lung pathology (*24*) but no weight loss or death (Fig. 4E and F). However, intraventricular administration of SARS-CoV-2 resulted in significant weight loss and death, even at the challenge virus dose 100-fold lower than that used for intranasal infection (Fig. 4E and F). Altogether, this highlights the neuro-replicative potential and lethal consequences of SARS-CoV-2 CNS infection in mice.

Discussion

We have demonstrated the potential for SARS-CoV-2 to infect neural tissues of both mice and human origin and demonstrate potential consequences of its neuroinvasion. Our results suggest that neurologic symptoms associated with COVID-19 may be related to consequences of direct viral invasion of the CNS. Although our rodent model does not utilize the endogenous ACE2 expression (Fig. 4), which may have a different tropism than what we observed, it has been previously reported that even mouse adapted SARS-CoV is still neurotropic in wild type mice and SARS-CoV-2 is neurotropic in mice with hACE2 expression from the endogenous locus (*25, 26*). Our work experimentally demonstrates that the brain is a site for high replicative potential for SARS-CoV-2. Given the nasal cavity to CNS connection through the cribriform plate, olfactory epithelium and nerve, the brain should be considered a high-risk organ system upon respiratory exposure (*27, 28*). We further show that SARS-CoV-2 causes significant neuronal death in human brain organoids (Fig. 2). Using electron microscopy, we identified viral particles budding from the endoplasmic reticulum, indicating the virus's ability to use the neuron cell machinery to replicate. Similar to neuronal loss observed in patient autopsies (*2*), we noticed large numbers of cells dying in the organoid, however, this neuronal death did not colocalize directly with virus infection (Fig. 2E). Single-cell RNA sequencing of the infected organoids showed metabolic changes in neurons without interferon or ISG signatures, indicating the neuroinvasive consequence of SARS-CoV-2 is unique compared to other neurotropic viruses such as ZIKV. Closer examination showed diverging metabolic changes in infected versus neighboring cells, suggesting that the infected cells can cause local changes to their microenvironment affecting survival of nearby cells. It is possible that viral infection induces locally hypoxic regions which aids in lowering the threshold for tissue damage in the context of an already oxygen deprived state. Whether or not locally induced hypoxia is present in patients or in mice remains to be investigated. Given the evidence of acute hypoxic ischemic damage without microthrombi in post-mortem brain of COVID-19 patients (*2*), our observations suggest a possible avenue to SARS-CoV-2 induced neuropathology.

While ACE2 expression levels in the human brain are still being investigated, we showed that ACE2 is functionally required for SARS-CoV-2 infection in human brain organoids. Further, we detected robust antiviral antibody presence in the CSF of a COVID-19 patient, who presented with acute neurologic symptoms. This finding suggests that, at least in some patients with COVID-19 and neurological symptoms, there is robust antibody response to the virus within the CSF. Although we did not find induction of ISGs in brain organoids, the neuroinflammatory consequences of SARS-CoV-2 cannot be excluded given the amount of cell death we observed.

In the in vivo setting of the CNS with vasculature and immune cells, neuronal death could have cascading downstream effects in causing and amplifying CNS inflammation. To gain a fuller understanding of the SARS-CoV-2 interaction within the CNS, it will be important to evaluate these possibilities in the future with imaging or autopsy analysis of the brain from COVID-19 patients. Altogether, our study provides clear demonstration that neurons can become a target of SARS-CoV-2 infection, with devastating consequences of cell death and neuronal damage.

References

1. L. Mao *et al.*, Neurologic Manifestations of Hospitalized Patients With Coronavirus Disease 2019 in Wuhan, China. *JAMA Neurol*, (2020).
2. I. H. Solomon *et al.*, Neuropathological Features of Covid-19. *N Engl J Med*, (2020).
3. V. G. Puelles *et al.*, Multiorgan and Renal Tropism of SARS-CoV-2. *N Engl J Med*, (2020).
4. L. Cantuti-Castelvetri *et al.*, Neuropilin-1 facilitates SARS-CoV-2 cell entry and provides a possible pathway into the central nervous system. *bioRxiv*, (2020).
5. N. D. Amin, S. P. Pasca, Building Models of Brain Disorders with Three-Dimensional Organoids. *Neuron* **100**, 389-405 (2018).
6. X. Qian *et al.*, Brain-Region-Specific Organoids Using Mini-bioreactors for Modeling ZIKV Exposure. *Cell* **165**, 1238-1254 (2016).
7. L. Pellegrini *et al.*, Human CNS barrier-forming organoids with cerebrospinal fluid production. *Science*, (2020).
8. S. Velasco *et al.*, Individual brain organoids reproducibly form cell diversity of the human cerebral cortex. *Nature* **570**, 523-527 (2019).
9. A. Ramani *et al.*, SARS-CoV-2 targets cortical neurons of 3D human brain organoids and shows neurodegeneration-like effects. *bioRxiv*, (2020).
10. S. Kanton *et al.*, Organoid single-cell genomic atlas uncovers human-specific features of brain development. *Nature* **574**, 418-422 (2019).
11. B. Cakir *et al.*, Engineering of human brain organoids with a functional vascular-like system. *Nat Methods* **16**, 1169-1175 (2019).
12. M. Watanabe *et al.*, Self-Organized Cerebral Organoids with Human-Specific Features Predict Effective Drugs to Combat Zika Virus Infection. *Cell Rep* **21**, 517-532 (2017).
13. D. Blanco-Melo *et al.*, Imbalanced Host Response to SARS-CoV-2 Drives Development of COVID-19. *Cell* **181**, 1036-1045 e1039 (2020).
14. B. P. Daniels *et al.*, The Nucleotide Sensor ZBP1 and Kinase RIPK3 Induce the Enzyme IRG1 to Promote an Antiviral Metabolic State in Neurons. *Immunity* **50**, 64-76 e64 (2019).
15. B. Yordy, N. Iijima, A. Huttner, D. Leib, A. Iwasaki, A neuron-specific role for autophagy in antiviral defense against herpes simplex virus. *Cell Host Microbe* **12**, 334-345 (2012).
16. H. Xia, E. Lazartigues, Angiotensin-converting enzyme 2 in the brain: properties and future directions. *J Neurochem* **107**, 1482-1494 (2008).
17. M. Hoffmann *et al.*, SARS-CoV-2 Cell Entry Depends on ACE2 and TMPRSS2 and Is Blocked by a Clinically Proven Protease Inhibitor. *Cell* **181**, 271-280 e278 (2020).
18. J. L. Daly *et al.*, Neuropilin-1 is a host factor for SARS-CoV-2 infection. *bioRxiv* , (2020).
19. M. Y. Li, L. Li, Y. Zhang, X. S. Wang, Expression of the SARS-CoV-2 cell receptor gene ACE2 in a wide variety of human tissues. *Infect Dis Poverty* **9**, 45 (2020).
20. W. Sungnak *et al.*, SARS-CoV-2 entry factors are highly expressed in nasal epithelial cells together with innate immune genes. *Nat Med* **26**, 681-687 (2020).
21. F. Qi, S. Qian, S. Zhang, Z. Zhang, Single cell RNA sequencing of 13 human tissues identify cell types and receptors of human coronaviruses. *Biochem Biophys Res Commun* **526**, 135-140 (2020).
22. P. B. McCray, Jr. *et al.*, Lethal infection of K18-hACE2 mice infected with severe acute respiratory syndrome coronavirus. *J Virol* **81**, 813-821 (2007).
23. J. Netland, D. K. Meyerholz, S. Moore, M. Cassell, S. Perlman, Severe acute respiratory syndrome coronavirus infection causes neuronal death in the absence of encephalitis in mice transgenic for human ACE2. *J Virol* **82**, 7264-7275 (2008).
24. B. Israelow *et al.*, Mouse model of SARS-CoV-2 reveals inflammatory role of type I interferon signaling. *bioRxiv*, (2020).

25. A. Roberts *et al.*, A mouse-adapted SARS-coronavirus causes disease and mortality in BALB/c mice. *PLoS Pathog* **3**, e5 (2007).
26. S. H. Sun *et al.*, A Mouse Model of SARS-CoV-2 Infection and Pathogenesis. *Cell Host Microbe*, (2020).
27. A. M. Baig, E. C. Sanders, Potential Neuroinvasive Pathways of SARS-CoV-2: Deciphering the Spectrum of Neurological Deficit Seen in Coronavirus Disease 2019 (COVID-19). *J Med Virol*, (2020).
28. T. Coolen *et al.*, Early postmortem brain MRI findings in COVID-19 non-survivors. *Neurology*, (2020).
29. M. A. Lancaster *et al.*, Cerebral organoids model human brain development and microcephaly. *Nature* **501**, 373-379 (2013).
30. M. A. Lancaster, J. A. Knoblich, Generation of cerebral organoids from human pluripotent stem cells. *Nat Protoc* **9**, 2329-2340 (2014).

Methods

All procedures were performed in a BSL-3/ABSL-3 facility (for SARS-CoV-2-related work) with approval from the Yale Environmental Health and Safety committee (#20-19 and #18-16).

Mice. Six to twelve-week-old mixed sex C57Bl/6 (B6J) purchased from Jackson laboratories, and B6.Cg-Tg(K18-ACE2)2Prlmn/J(K18-hACE2) mice (gift from Jackson Laboratories) were subsequently bred and housed at Yale University. All procedures used in this study (sex-matched, age-matched) complied with federal guidelines and the institutional policies of the Yale School of Medicine Animal Care and Use Committee.

AAV infection (Intratracheal and Intracisternal magna injection). Adeno-associated virus 9 encoding hACE2 were purchased from Vector biolabs (AAV-CMV-hACE2).

Intratracheal injection. Animals were anaesthetized using a mixture of ketamine (50 mg kg^{-1}) and xylazine (5 mg kg^{-1}), injected intraperitoneally. The rostral neck was shaved and disinfected. A 5mm incision was made and the salivary glands were retracted, and trachea was visualized. Using a 500µL insulin syringe a 50µL bolus injection of 10^{11}GC of AAV-CMV-hACE2 was injected into the trachea. The incision was closed with VetBond skin glue. Following intramuscular administration of analgesic (Meloxicam and buprenorphine, 1 mg kg^{-1}), animals were placed in a heated cage until full recovery.

Intracisternal magna injection. Mice were anesthetized using ketamine and xylazine, and the dorsal neck was shaved and sterilized. A 2 cm incision was made at the base of the skull, and the dorsal neck muscles were separated using forceps. After visualization of the cisterna magna, a Hamilton syringe with a 15 degree 33 gauge needle was used to puncture the dura. 3µL of AAV_9 (3.10^{12} viral particles/mouse) or mRNA (4-5 µg) was administered per mouse at a rate of 1µL min^{-1}. Upon completion of the injection, needle was left in to prevent backflow for an additional 3 minutes. The skin was stapled, disinfected and same post-operative procedures as intratracheal injections were performed.

Generation of SARS-CoV-2 virus. To generate SARS-CoV-2 viral stocks, Huh7.5 cells were inoculated with SARS-CoV-2 isolate USA-WA1/2020 (BEI Resources #NR-52281) to generate a P1 stock. To generate a working stock, VeroE6 cells were infected at a MOI 0.01 for four days. Supernatant was clarified by centrifugation (450g x 5min) and filtered through a 0.45 micron filter.

To concentrate virus, one volume of cold (4 °C) 4x PEG-it Virus Precipitation Solution (40% (w/v) PEG-8000 and 1.2M NaCl) was added to three volumes of virus-containing supernatant. The solution was mixed by inverting the tubes several times and then incubated at 4 °C overnight. The precipitated virus was harvested by centrifugation at 1,500 x g for 60 minutes at 4 °C. The pelleted virus was then resuspended in PBS then aliquoted for storage at -80°C. Virus titer was determined by plaque assay using Vero E6 cells.

SARS-CoV-2 infection of organoids. Brain organoids in low adhesion plates were infected with SARS-CoV-2 at a MOI of 1.

SARS-CoV-2 infection (intranasal). Mice were anesthetized using 30% v/v Isoflurane diluted in propylene glycol. Using a pipette, 50µL of SARS-CoV-2 ($3x10^7$ PFU/ml) was delivered intranasally.

SARS-CoV-2 infection (intraventricular). Animals were anaesthetized using a mixture of ketamine (50 mg kg^{-1}) and xylazine (5 mg kg^{-1}), injected intraperitoneally. After sterilization of the scalp with alcohol and betadine, a midline scalp incision was made to expose the coronal and sagittal sutures, and a burr holes were drilled 1 mm lateral to the sagittal suture and 0.5 mm posterior to the bregma. A 10 µl Hamilton syringe loaded with virus, and was inserted into the burr hole at a depth of 2 mm from the surface of the brain and left to equilibrate for 1 min before infusion. Once the infusion was finished, the syringe was left in place for another minute before removal of the syringe. Bone wax was used to fill the burr hole and skin was stapled and cleaned. Following intramuscular administration of analgesic (Meloxicam and buprenorphine, 1 mg kg^{-1}), animals were placed in a heated cage until full recovery. For high condition, 5µL of SARS-CoV-2 ($3x10^7$ PFU/ml) and for low condition 5µL of SARS-CoV-2 ($3x10^6$ PFU/ml) was used.

Viral RNA analysis. At indicated time points mice were euthanized in 100% Isoflurane. Brain tissue was placed in a bead homogenizer tube with 1ml of PBS+2%FBS. After homogenization 250ul of this mixture was placed in 750ul Trizol LS (Invitrogen), and RNA was extracted with RNeasy mini kit (Qiagen) per manufacturer protocol. To quantify SARS-CoV-2 RNA levels, RT-qPCR was performed using Luna Universal Probe Onestep RT-qPCR kits (New England

Biolabs) with 1 ug of RNA, with the US CDC real-time RT-PCR primer/probe sets for 2019-nCoV_N1.

Viral titer. Brain homogenates were centrifuged at 3900g for 10 minutes and supernatant was taken for plaque assays. Supernatant at limiting dilutions were incubated on Vero E6 cells in MEM supplemented $NaHCO_3$, 4% FBS 0.6% Avicel RC-581. Plaques were resolved at 48hrs post infection by fixing in 10% formaldehyde for 1 hour followed by staining for 1 hour in 0.5% crystal violet in 20% ethanol.

Stem cell culture. Human Y6 and Y1 iPS lines were obtained from Yale Stem Cell Center and New York Cell Stem Foundation respectively. Cells were verified as being pluripotent, having normal karyotype, mycoplasma free and cultured in feeder-free conditions on matrigel-coated plates with mTeSR Plus culture media (Stem Cell Technologies) and passaged using ReLeSR (Stem Cell Technologies).

Teratoma formation. $1x10^6$ Y6 iPSC cells were collected by collagenase treatment, and resuspended in 100 ml of DMEM/F12, collagen, and matrigel mix (2:1:1 ratio). Cells were intramuscularly injected into immunodeficient Rag2-/-GammaC-/- mouse. After 8 weeks, teratomas were harvested, fixed, and subjected to paraffin-embedding and haematoxylin and eosin (H/E) staining.

G-band staining for Karyotype analysis. Y6 iPSC small clumps were seeded on glass slide pre-coated with Matrigel and fed with mTESR medium for three days. Then, medium were switched to DMEM basal medium supplemented with 10% of FBS for another 3 days. Then the slide was transferred to Yale Cytogenetic laboratory for G-band staining.

Neural Progenitor Cell culture. Y6 iPS lines were differentiated to NPCs on matrigel-coated plates using the monolayer protocol of the StemDiff SMADI Neural Induction kit (Catalog # 08581, Stem Cell Technologies) for two passages and then maintained in StemDiff Neural Progenitor media (Catalog #05833, Stem Cell Technologies). Twelve-day NPCs were used for all experiments.

Cerebral organoid culture. For preparation of embryoid bodies, 9000 single cells were seeded in each well of low attachment 96-well U-bottom plate and 10 μM Y-27632 ROCK inhibitor for

one day. Cerebral organoids were generated following exactly the previously established protocol(*29, 30*), using an orbital shaker for agitation.

Immunostaining. Brains of infected mice and organoids were collected and fixed in 4% PFA. Samples were then dehydrated in a 30% sucrose solution. Cryostat sections were blocked in 0.1 M Tris-HCl buffer with 0.3% Triton and 1% FBS before staining. Slides were stained for IBA-1 (nb100-1028, Novus Biologicals), GFAP (ab4674, abcam and rabbit anti-SARS-CoV-2 nucleocapsid (GeneTex) Slides were mounted with Prolong Gold Antifade reagent (Thermo fisher). All slides were analyzed by fluorescence microscopy (BX51; Olympus).

Organoids were fixed in 4% PFA in a BSL3 facility then moved to 30% sucrose solution at 4°C for at least 24h. Organoids were then embedded in Tissue Freezing Medium (TFM) and cut into 20 µm sections using a cryostat and mounted on slides. After blocking and permeabilization with 0.25% Triton-X 100 and 4% donkey serum, sections were incubated overnight with primary antibody: ms anti-Sox2 (1:500, Santa Cruz, sc-365823), rat anti-CTIP2 (1:500, Abcam, ab18465), ms anti-MAP2 (1:500, Millipore, MAB3418), rb anti-SARS-CoV-2 nucleocapsid (1:250, GeneTex, GTX635679),rb anti-HIF1 alpha antibody (Genetex, GTX127309). TUNEL assay was performed using the Click-It Plus TUNEL Assay for In Situ Apoptosis Detection (Thermofisher, C10617) per the manufacturer's instructions. Alexa Fluor 488, 555, 647 antibodies were applied for 1hr at room temperature (1:500) after three 10min PBS washes. To mark nuclei, DAPI (1:3000) was added to the secondary antibody incubation. Slides were then washed three times in PBS and then mounted with VectaShield Anti-Fade Mounting Medium. Images were acquired using a Zeiss LSM 880 confocal microscope (Carl Zeiss) and prepared using Fiji (NIH).

Neural progenitor cells on coverslips were fixed in 4% PFA for 15 minutes at room temperature in BSL3 conditions and washed 3x with PBS. After blocking and permeabilization with 0.25% Triton-X 100 and 10% donkey serum, coverslips were incubated overnight with primary antibody as described above. TUNEL assay was performed as described above. Alexa Flour 488, 555, and 647 antibodies were applied for 1hr at room temperature (1:500) after three 10min PBS washes. Coverslips were then washed three times in PBS and then mounted on slides with Prolong Diamond Anti-Fade Mountant with DAPI (Thermofisher). Images were acquired using a Zeiss LSM 880 confocal microscope (Carl Zeiss) and prepared using Fiji (NIH).

Electron microscopy. Organoids were fixed using 2.5% glutaraldehyde in 0.1M phosphate buffer, osmicated in 1% osmium tetroxide, and dehydrated in ethanol. During dehydration, 1% uranyl acetate was added to the 70% ethanol to enhance ultrastructural membrane contrast. After dehydration the organoids were embedded in Durcupan and 70 nm sections were cut on a Leica ultramicrotome, collected on Formvar coated single-slot grids, and imaged on a Tecnai 12 Biotwin electron microscope (FEI).

Single-cell RNA-seq. Organoids were collected and single cell suspensions were made using a papain dissociation system (Worthington Biochemical Corporation). Single-cell suspensions were loaded onto the Chromium Controller (10x Genomics) for droplet formation. scRNA-seq libraries were prepared using the Chromium Single Cell 3′ Reagent Kit (10x Genomics. Samples were sequenced on the on the NovaSeq.

R v.3.4.2 (R Core Team 2013) was used for all statistical analysis. Sequencing results were demultiplexed into Fastq files using the Cell Ranger (10x Genomics, 3.0.2) mkfastq function. Samples were aligned to GRCh38 10x genome. The count matrix was generated using the count function with default settings. Matrices were loaded into Seurat v.3. 1.5 for downstream analysis. Cells with less than 200 unique molecular identifiers, or high mitochondrial content were discarded. Using FindIntegrationAnchors and IntegrateData functions, all libraries were integrated into a single matrix. Principal component values that were statistically significant were identified, and a cut-off point was determined using the inflection point after using the PCElbowPlot function. Clusters were determined using the RunUMAP, FindNeighbors, and FindClusters functions on Seurat. Cells were considered infected if transcripts aligned to viral ORF1ab, Surface glycoprotein (S), ORF3a, Envelope protein (E), Membrane glycoprotein (M), ORF6, ORF7a, ORF8, Nucleocapsid phosphoprotein (N) or ORF10. Differentially expressed genes from the FindMarkers function were used to perform PANTHER-GO statistical over-representation tests for up-regulated and downregulated genes in each condition shown in Fig. 2F and G. Gene lists for Fig. 2H were obtained from GSEA databases (gsea-msigdb.org/gsea/index.jsp).

ACE2 blocking. For ACE2 blocking assays, Organoids were preincubated with anti-ACE2 Antibodies (AF933, R&D Systems) or isotype antibodies at a concentration of 100ug/mL for 1 hour at 4 degrees. Organoids were then infected with SARS-CoV-2 as described above.

CSF neutralization assay. Excess CSF was obtained from a hospitalized patient with COVID-19 who underwent clinical LP, and from a healthy control volunteer. CSF was centrifuged to isolate cell-free supernatant, which was used for ELISA and neutralization assays as follows:

Enzyme-linked immunosorbent assay. ELISAs were performed as previously reported (*24*). In short, Triton X-100 and RNase A were added to serum samples at final concentrations of 0.5% and 0.5mg/ml respectively and incubated at room temperature (RT) for 3 hours before use to reduce risk from any potential virus in serum. 96-well MaxiSorp plates (Thermo Scientific #442404) were coated with 50 µl/well of recombinant SARS Cov-2 S1 protein (ACROBiosystems #S1N-C52H3-100ug) at a concentration of 2 µg/ml in PBS and were incubated overnight at 4 °C. The coating buffer was removed, and plates were incubated for 1h at RT with 200µl of blocking solution (PBS with 0.1% Tween-20, 3% milk powder). Serum was diluted 1:50 in dilution solution (PBS with 0.1% Tween-20, 1% milk powder) and 100µl of diluted serum was added for two hours at RT. Plates were washed three times with PBS-T (PBS with 0.1% Tween-20) and 50µl of mouse IgG-specific secondary antibody (BioLegend #405306, 1:10,000) diluted in dilution solution added to each well. After 1h of incubation at RT, plates were washed three times with PBS-T. Samples were developed with 100µl of TMB Substrate Reagent Set (BD Biosciences #555214) and the reaction was stopped after 15 min by the addition of 2 N sulfuric acid.

Neutralization assay. Virus for infection was preincubated with 500µL of healthy or COVID19 CSF in 37 degrees for one hour before infection of organoids. The Organoid culture was supplemented with an additional 500µL of CSF after infection until the organoid was collected for imaging.

Human subjects. Research participants were enrolled at Yale University through Human Investigation Committee Protocols HIC#2000027690 and HIC #1502015318. The Institutional Review Board at Yale approved the protocols, and informed consent was obtained from all participants.

Statistical analysis. No statistical methods were used to predetermine sample size. The investigators were not blinded during experiments and outcome assessment, but outcome assessment was additionally evaluated by animal technicians and vets blinded to the study.

Survival curves were analyzed using a log-rank (Mantle-Cox) test. For other data, normally distributed continuous variable comparisons used a two-tailed unpaired Student's *t*-test or paired Student's *t*-test with Prism software.

Acknowledgements

We thank Yale Environmental Health and Safety (EHS) department for allowing safe working environments with the SARS-CoV-2 virus. We also thank the patient donors, and clinicians who helped with the collection of CSF for neutralization assays. We also thank the members of YCGA who have helped with all aspects of sequencing. Finally, we thank the members of the Iwasaki lab for insightful discussions regarding the project. This study was supported by awards from National Institute of Health grants, T32GM007205 (MSTP training grant), F30CA239444 (to ES), 2T32AI007517-16 (to BI), K23MH118999 (to SFF) Women's Health Research at Yale Pilot Project Program (AI, AR), Fast Grant from Emergent Ventures at the Mercatus Center (AI, ES, CBW), Mathers Foundation (AR, CBW, AI), and the Ludwig Family Foundation (AI, AR, CBW). A.I. is an investigator of the Howard Hughes Medical Institute.

Author Contributions

E. S, C.Z., K.B., and A.I. planned the project and analyzed data. E.S., C.Z. and A.I. wrote the manuscript. E.S., C.Z., B.I. performed experiments. P.L., O.E.W., F.L., Y.D., K.S.B., Y.Y., G.W., J.H., E.N., J.W., M.M.A, assisted with experiments. A.R., C.B.W., T.L.H., A.L., S.F.F., and K.B. provided expertise and materials for analysis of data.

Competing Interests

None of the authors declare interests related to the manuscript.

Materials & Correspondence

Correspondence and material requests should be addressed to akiko.iwasaki@yale.edu and kaya.bilguvar@yale.edu

Requests for scripts, code and raw data used in this study should be addressed to eric.song@yale.edu

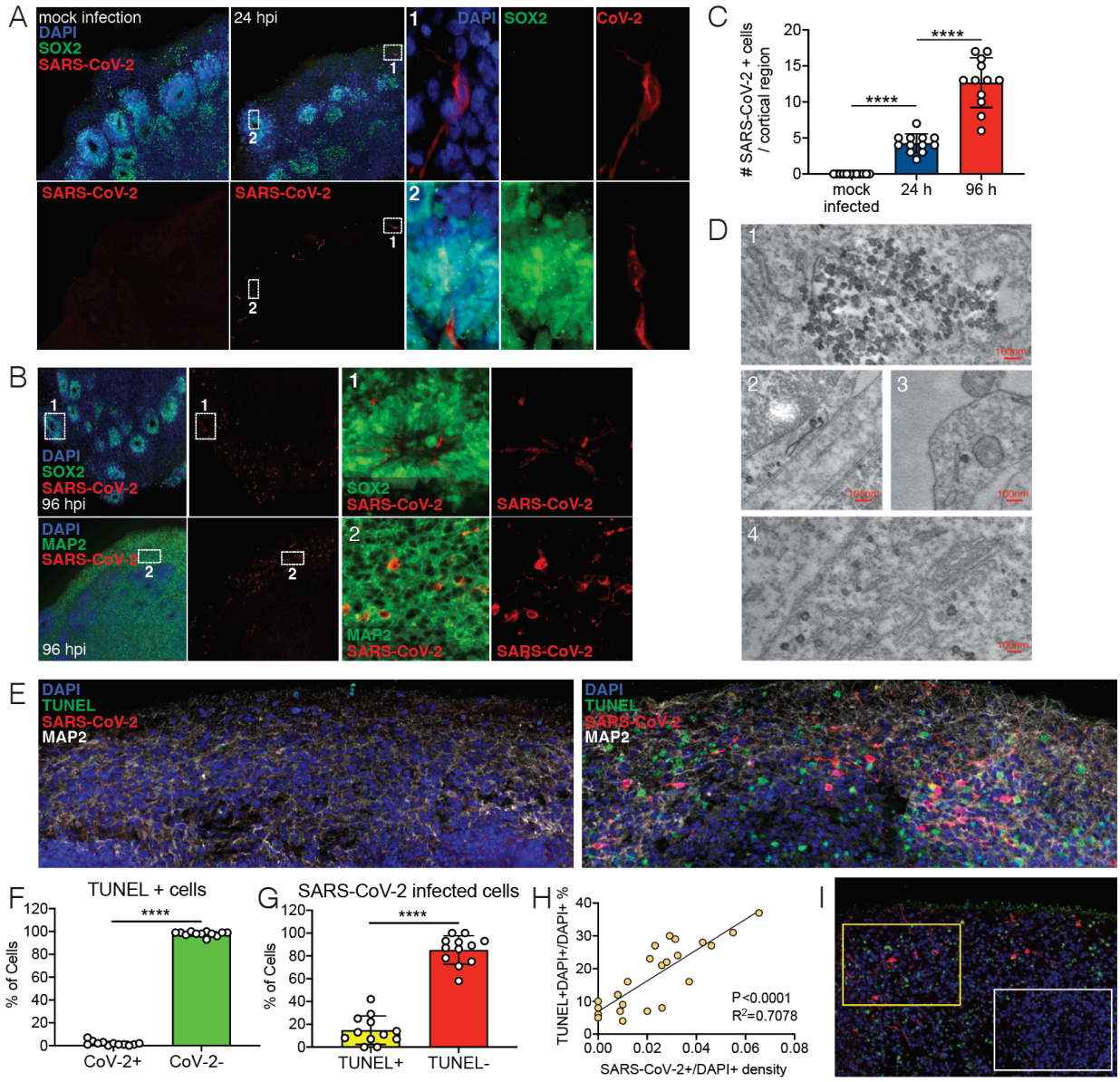

Fig. 1: SARS-CoV-2 infects human brain organoids and induces cell death. Human brain organoids were infected with SARS-CoV-2 and collected at 24 hours post infection (hpi) or 96 hpi to analyze for different cellular markers. (**A**) Images of brain organoids looking at SARS-CoV-2 infection (in red) 24 hpi (refer to fig. S2C for additional images). (**B**) Images of brain organoids looking at SARS-CoV-2 infection (in red) 96 hpi (refer to fig. S2D for additional images). (**C**) Quantification of SARS-CoV-2 positive cells in a cortical region of organoids (**A-B**). (**D**) Electron microscopy image of SARS-CoV-2 viral particles in brain organoids (refer to fig. S3 for uncropped and additional images). (**E**) Organoids were stained with TUNEL to evaluate cell death at 96hpi. (**F**) Quantification of SARS-CoV-2 and TUNEL double positive (yellow) or SARS-CoV-2 negative, TUNEL positive (green) cells over total TUNEL positive cells. (**G**) Quantification of SARS-CoV-2 and TUNEL double positive (yellow) or SARS-CoV-2 positive, TUNEL negative (red) cells over total SARS-CoV-2 positive cells. (**H**) Correlation between the frequency of TUNEL positive cells and presence SARS-CoV-2 in different regions of the organoid. (**I**) Representative image of TUNEL and SARS-CoV-2 staining showing high-density SARS-CoV-2 region (yellow box) and low-density SARS-CoV-2 region (white box) in the same plane. All experiments were performed with unique organoid n of 4 per condition, with images from n = 12 cortical regions with two IPSC lines, and student's t-test was performed (****, P<0.0001).

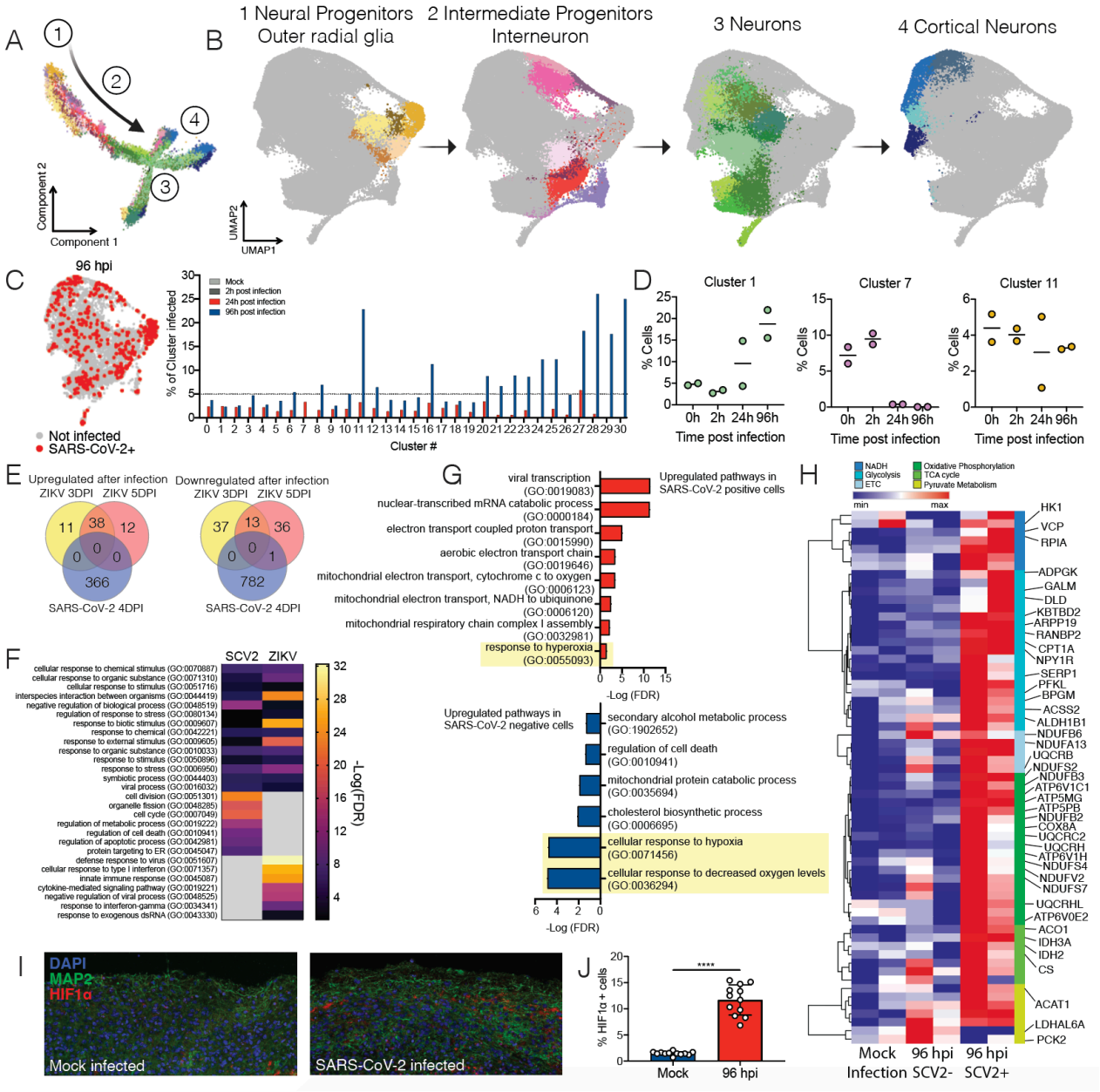

Fig. 2: Neuronal cells undergo a unique metabolic response to SARS-CoV-2 infections. Brain organoids were infected with SARS-CoV-2 and sequenced with 10x single cell sequencing strategies. (**A**) Monocle trajectory analysis resulted in four distinct states of cells from the organoid. (**B**) The four major clusters consisted of 1. Neural progenitor, outer radial glia like cells, 2. Intermediate progenitor, interneurons, 3. Neurons, and 4. Cortical neurons. For more detailed subtypes, refer to fig. **S4** and **S5**. (**C**) Projection of cells with SARS-CoV-2 transcripts (in red) onto the UMAP. Percentage of infected cells in each cluster. (**D**) Change in population representation of example clusters after infection (refer to fig. S4 for all clusters). (**E**) Differentially expressed genes (DEGs) from brain organoids infected with ZIKV (Watnabe et al 2017 Cell Reports) were compared with DEGs from SARS-CoV-2 infected organoids. (**F**) Enriched gene ontology terms (geneontology.com) for upregulated genes from (**E**). (**G**) Enriched GO terms in SARS-CoV-2 infected cells (top) and SARS-CoV-2 negative bystander cells from 96 hpi organoids (bottom). (**H**) Heatmap of genes from metabolic pathways. (**I**) HIF1A staining of brain organoids that were mock infected versus 96hpi. (**J**) Quantification of HIF1A positive cells in SARS-CoV-2 infected organoids. Single cell RNA-seq was performed in duplicates with one IPSC line (Y6). HIF1A staining was performed with unique organoid n of 4 per condition, with images from n = 12 cortical regions with two IPSC lines, and student's t-test was performed (****, P<0.0001).

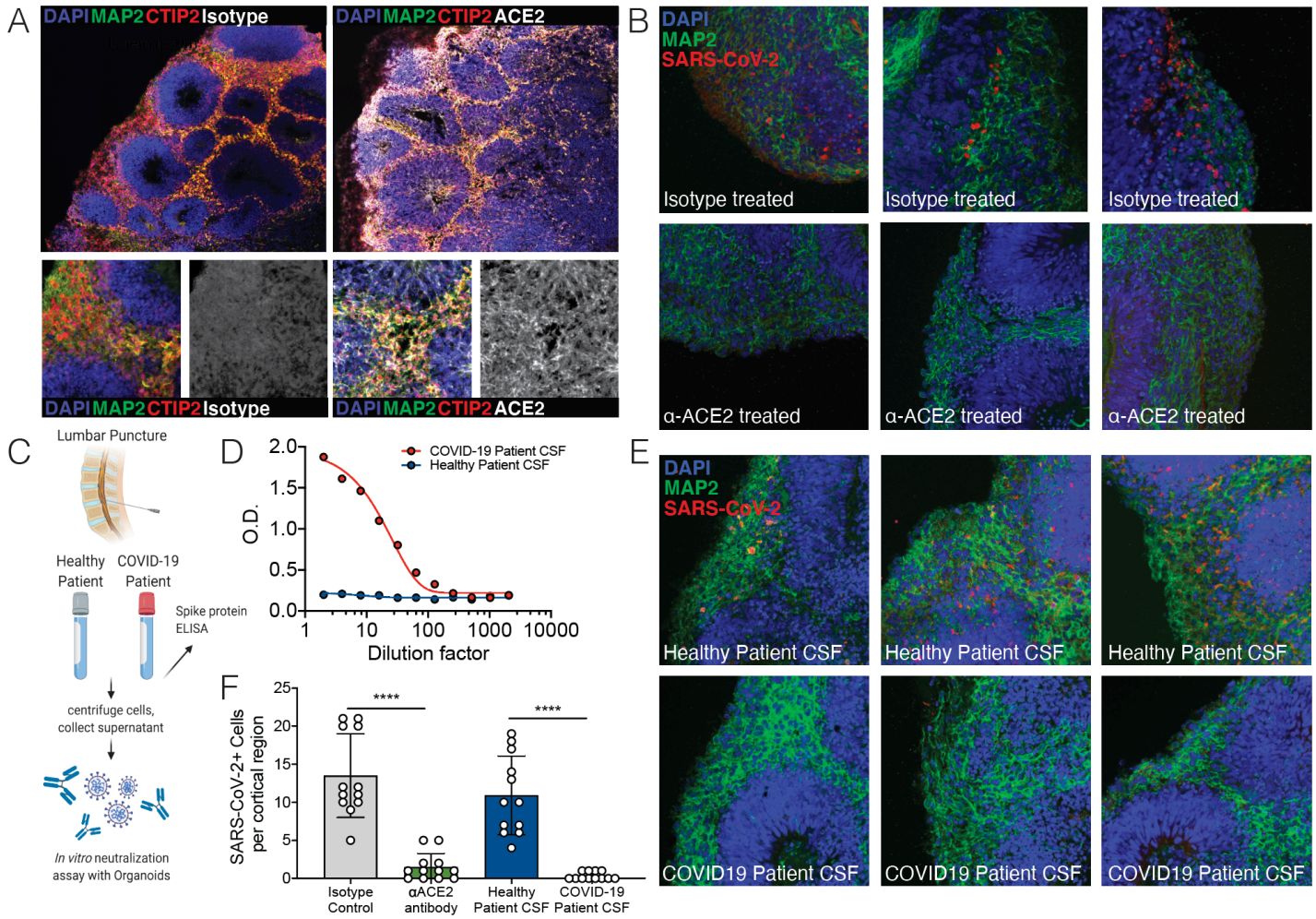

Fig. 3: SARS-CoV-2 neural infection depends on ACE2 and can be neutralized by anti-spike antibodies found in CSF of COVID-19 patients. (**A**) Immunofluorescence staining of ACE2 in brain organoids. (**B**) Immunofluroescence staining of organoids pre-incubated with isotype antibodies (top row) or anti-ACE2 antibodies (bottom row) and infected with SARS-CoV-2. (**C**) Schematic showing collection of clinical lumbar puncture from patients with and without COVID-19 for assays shown in (**D-F**). (**E**) Immunofluroescence staining of organoids infected with SARS-CoV-2 preincubated with CSF from health patients (top row) or CSF from COVID-19 patients (bottom row). (**F**) Quantification of figures from (**C** and **E**). All experiments were performed with unique organoid n of 4 per condition, with images from n = 12 cortical regions with two IPSC lines, and student's t-test was performed (****, P<0.0001).

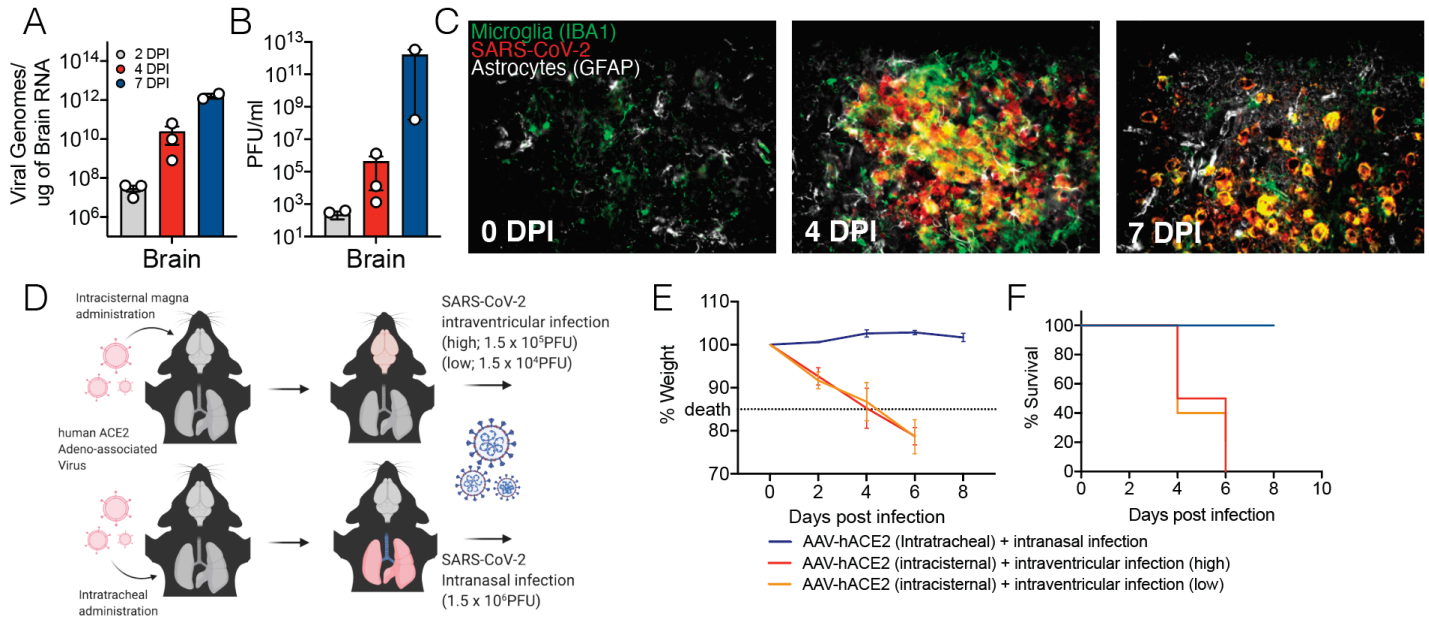

Fig. 4: SARS-CoV-2 replicates efficiently in the brain of mice and can cause central nervous system specific lethality. (**A-C**) Mice expressing human ACE2 under the K18 promoter (K18-hACE2) were infected with SARS-CoV-2 intranasally, and brains of the mice were collected at days 2, 4 and 6 post infection for (**A**) qPCR or (**B**) plaque assay, or (**C**) immunofluorescence imaging (2 DPI, n=3; 4 DPI, n=3; 7 DPI, n=2). (**D**) Schematic of experiment for (**E-F**), adeno-associated virus coding for human ACE2 (AAV-hACE2) were injected in to the cisterna magna or intratracheally to induce brain specific or lung specific expression of hACE2. Brain hACE2 expressing mice were infected with SARS-CoV-2 intraventricularly, and lung hACE2 expressing mice were infected with SARS-CoV-2 intranasally. (**E**) Weight loss curve and (**F**) survival curve of mice infected with SARS-CoV-2 in the lung (blue) and the brain (red and orange) (blue, n=10; red, n=4; orange, n=4).

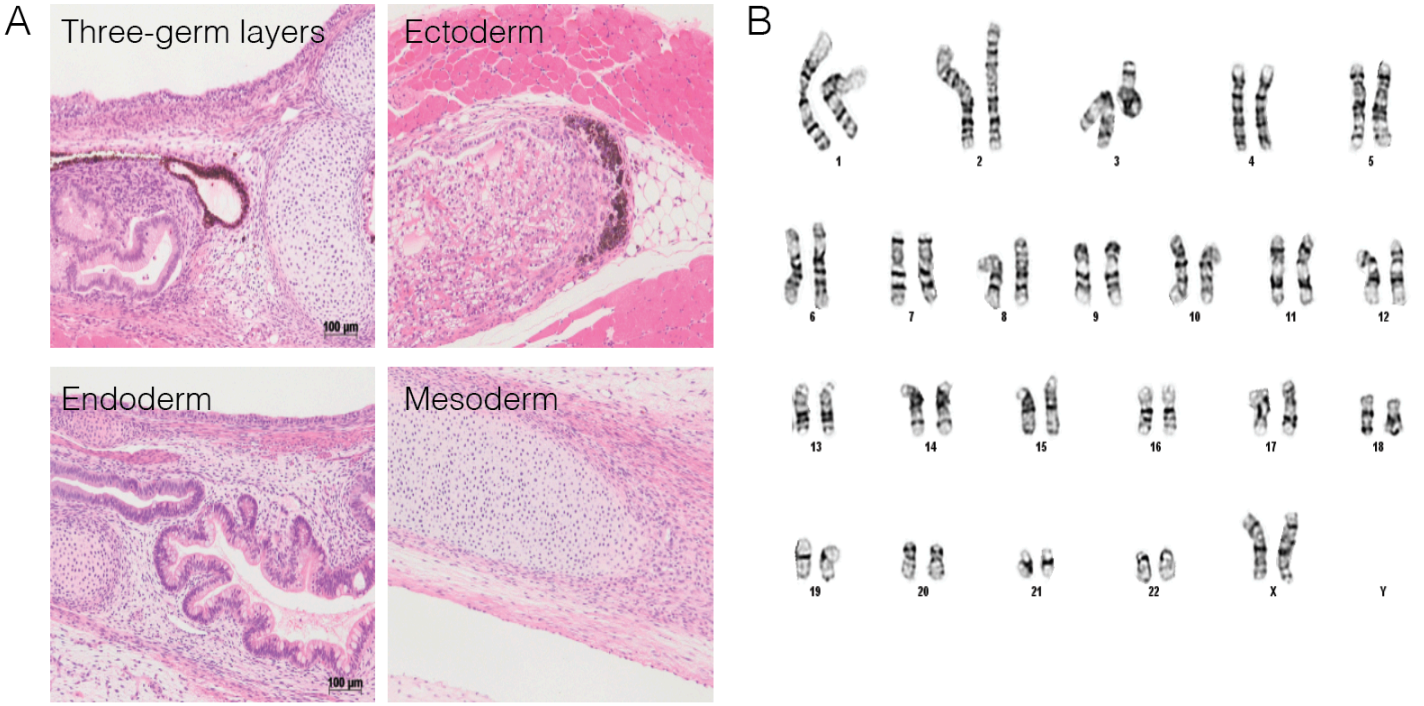

fig. S1: Pluripotency of Y6 line. (**A**) Sample images of cell types of three germ-layers in teratomas following transplantation to Rag2-/-GammaC-/- mice. Scale bar 100um. (**B**) Sample image showing normal karyotype for Y6 line.

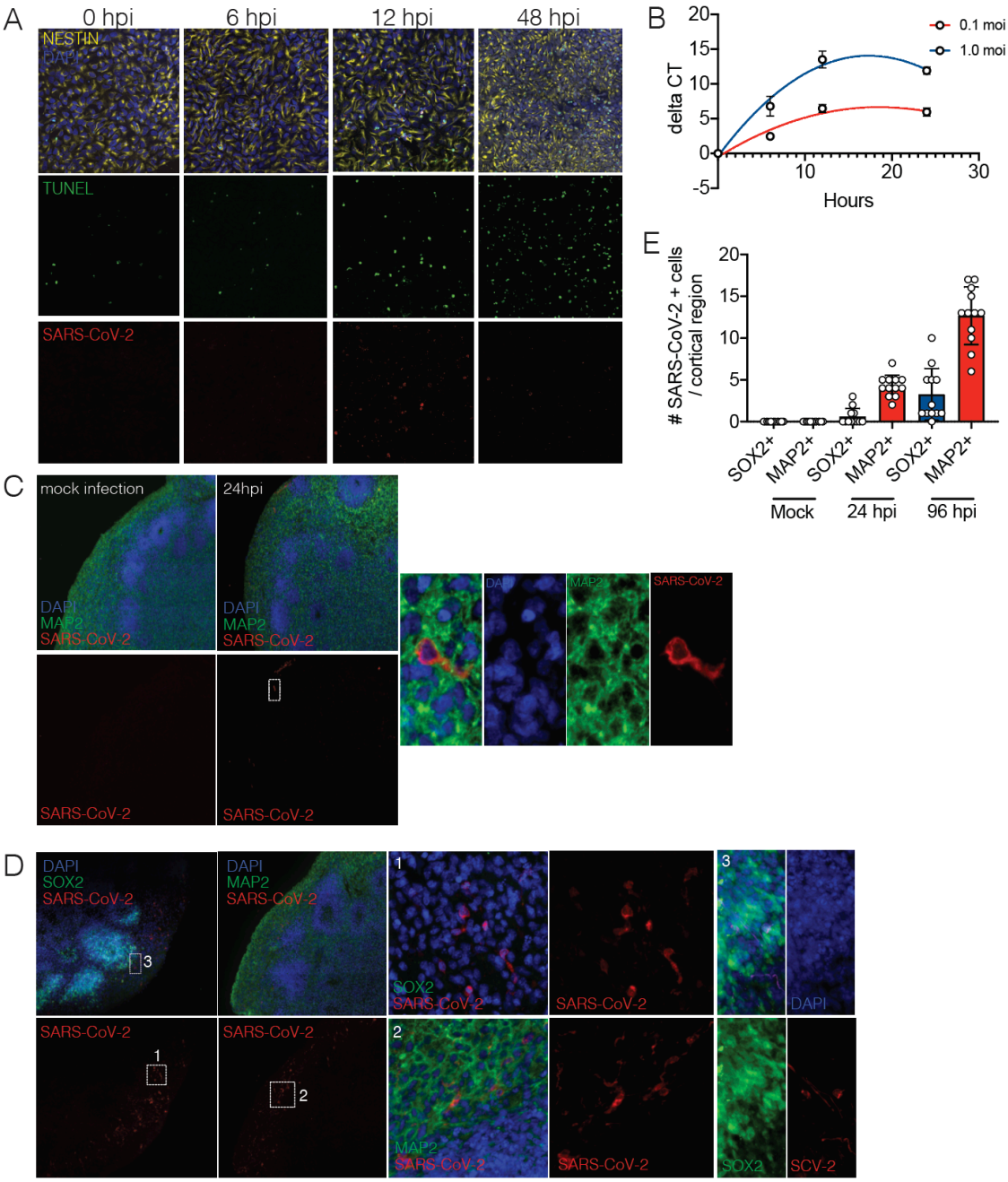

fig. S2: SARS-CoV-2 infection in hPSC-derived neural progenitor cells and 9-week organoids.
(**A**) Representative images of immunostaining of hNPCs with TUNEL staining, anti-Nestin, and anti-SARS-CoV-2 nucleocapsid antibody at 0, 6, 12, and 48 hours after infection. (**B**) RT-PCR amplification of COVID-genome from infected hNPC cells. (**C**) Sample images of immunostaining of 9-week organoids with DAPI, anti-MAP2, and anti SARS-CoV-2 ab at 24 hpi after SARS-CoV-2 or mock infection. Note the perinuclear and neuritic staining of SARS-CoV-2 in the MAP2+ cell. Dashed white box corresponds to SARS-CoV-2+ and MAP2+ single cell in 24 hpi organoid. (**D**) Sample images of immunostaining of 9-week organoids with DAPI, anti-MAP2 or anti-Sox2, and anti-SARS-CoV-2 ab at 96 hpi after SARS-CoV-2 or mock infection. Dashed white box "1" corresponds to "1 panel" showing magnified SARS-COV-2+/SOX2- cell in 96 hpi organoid. Dashed white box "2" corresponds to "2 panel" showing SARS-COV-2+ and MAP2+ cell in 96 hpi organoid. "3" panel shows SOX2+/SARS-CoV-2+ cell in 96 hpi organoid. (**E**) Quantification of number of SARS-CoV-2 + cells / cortical region that are either SOX2+ or MAP2+ in mock, 24 hpi, and 96 hpi, organoids. N=4 organoids per condition, 12 cortical regions from two iPSC lines.

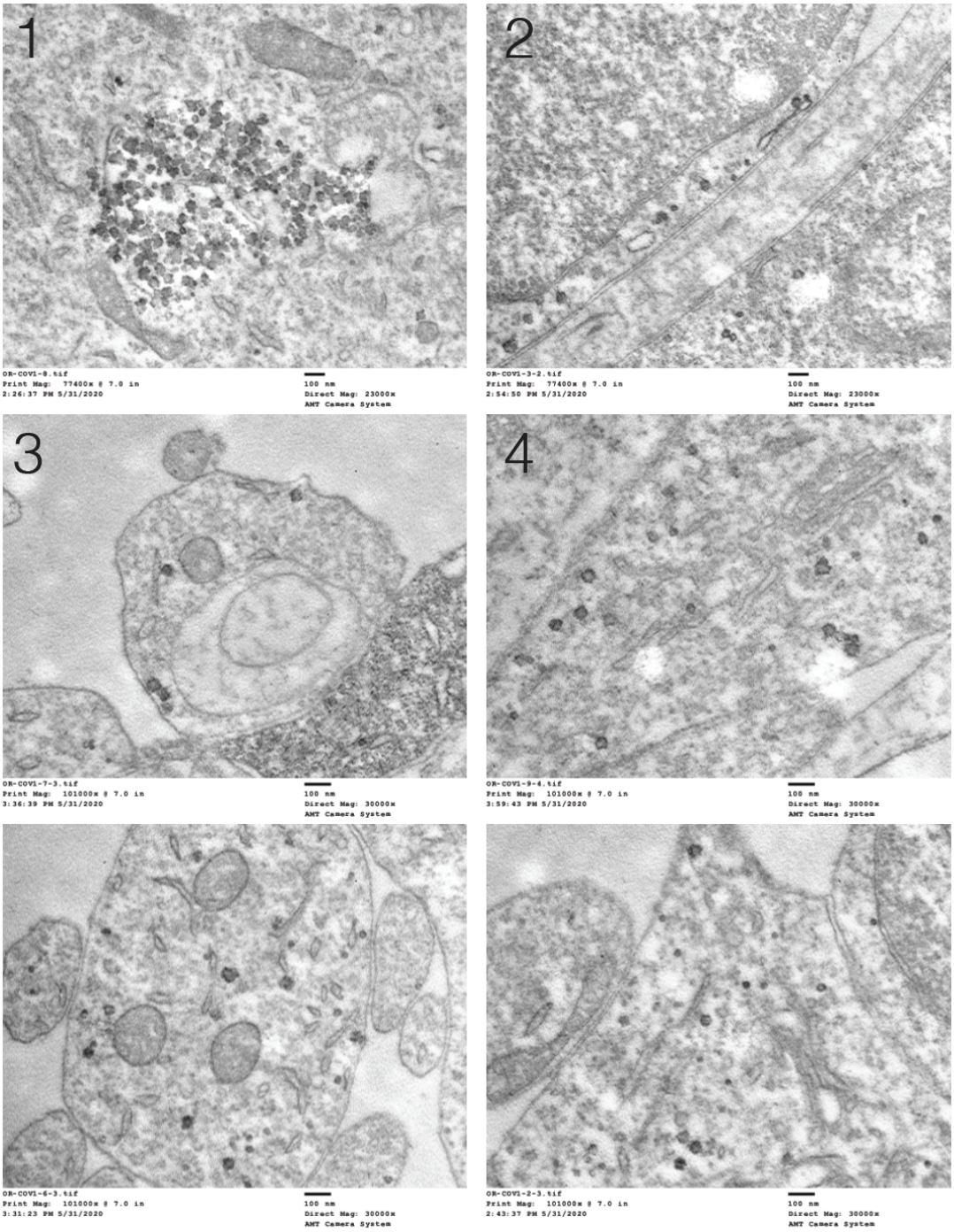

Fig. S3: Electron Microscopy of SARS-CoV-2 infection. Uncropped images of electron microscopy of infected brain organoids from Fig. 1D.

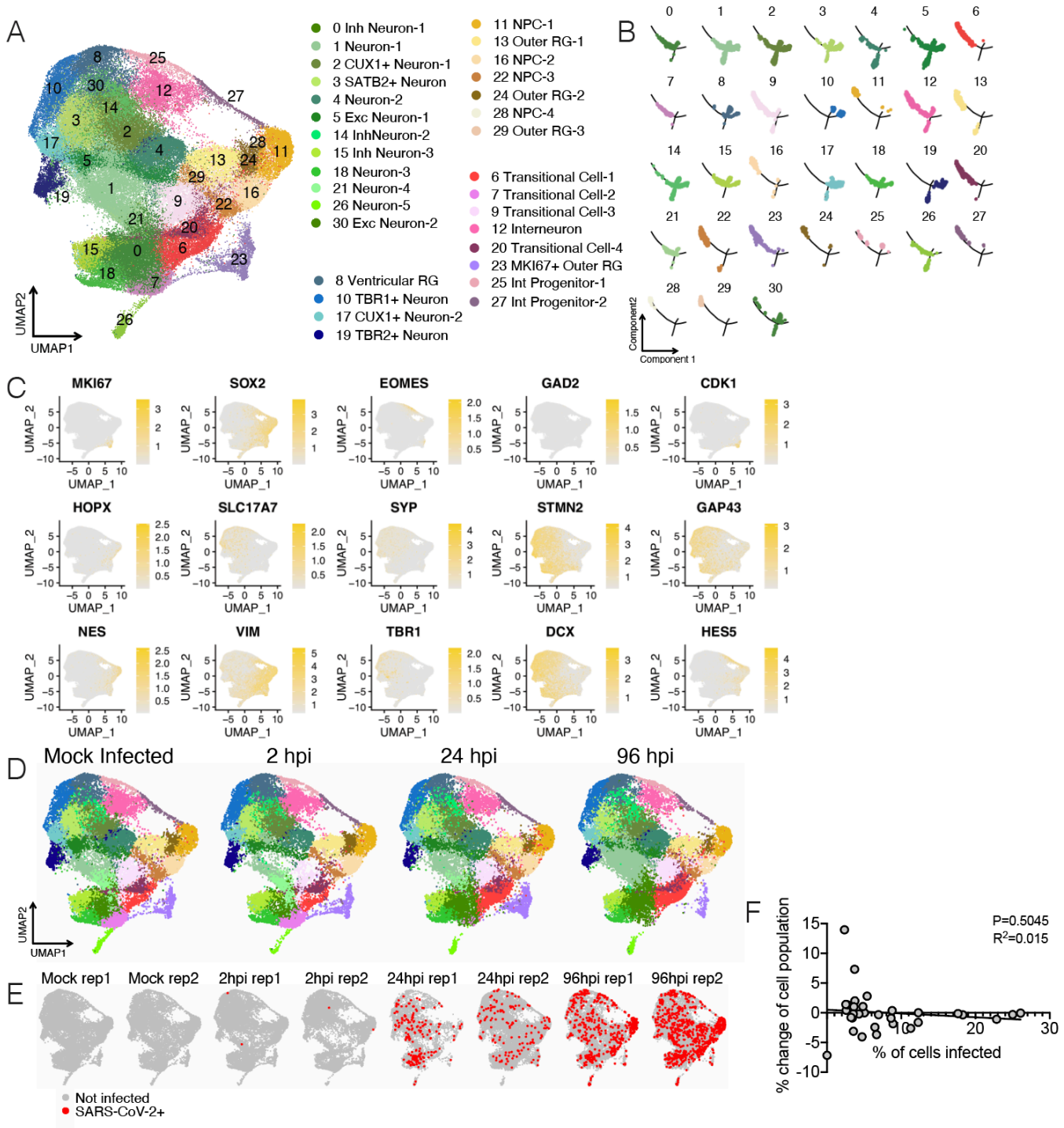

fig. S4: Single cell RNA-seq of SARS-CoV-2 infected organoids. (**A**) UMAP projection of cells from single cell sequencing. (**B**) Monocle projection of individual clusters. (**C**) Heatmap of commonly used genes for identification of cell subtypes in human brain organoids. (**D**) UMAP projection of organoids depending on infection status. (**E**) UMAP heatmap of SARS-CoV-2 transcript + cells separated by infection status. (**F**) Correlation between % change of cell population versus % of cells infected in each cluster.

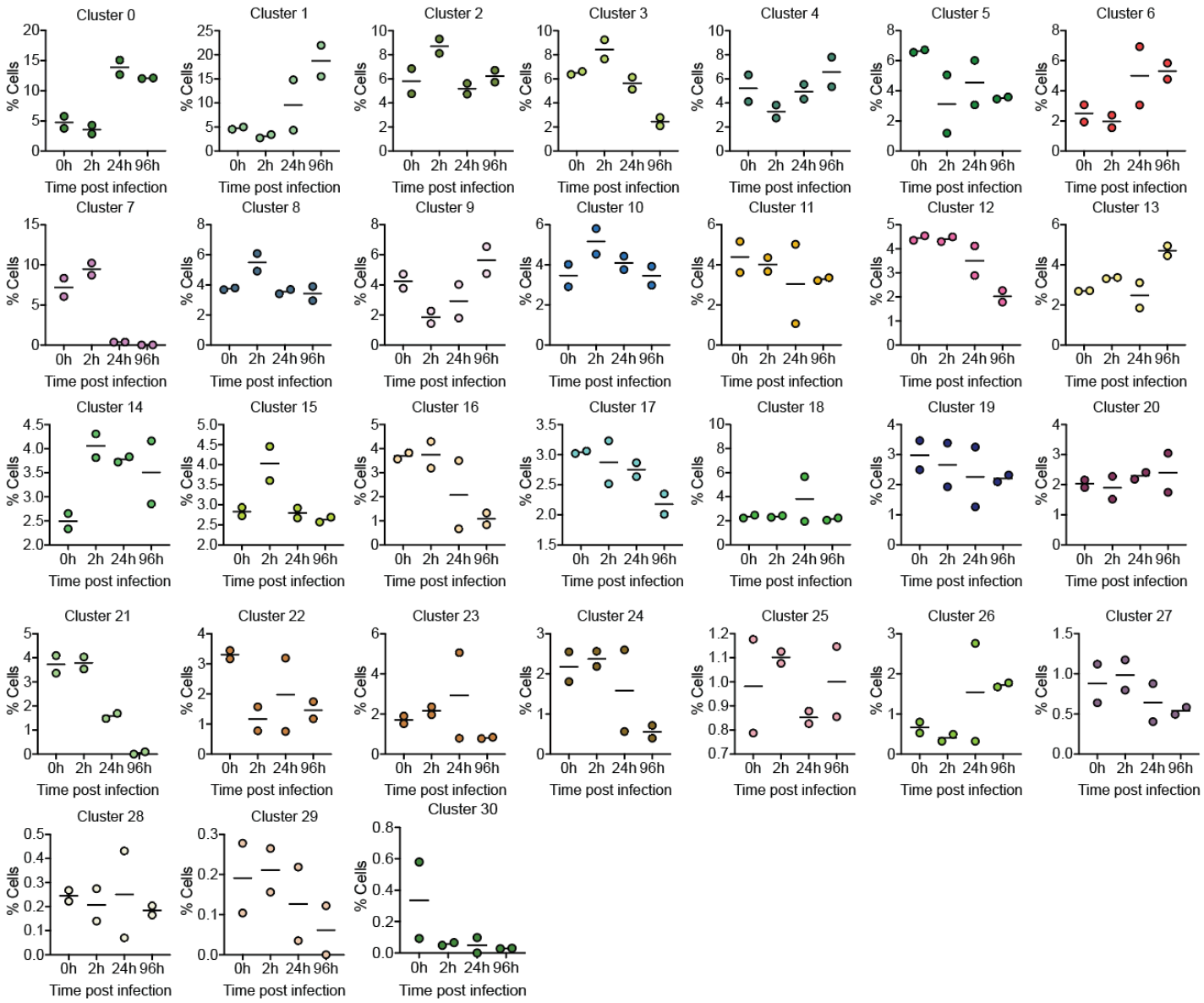

fig. S5: Frequency of each cell cluster from single cell RNA-seq. Graphs display the % frequency of each cluster during a given infection status, 0, 2, 24 and 96 hours post infection.

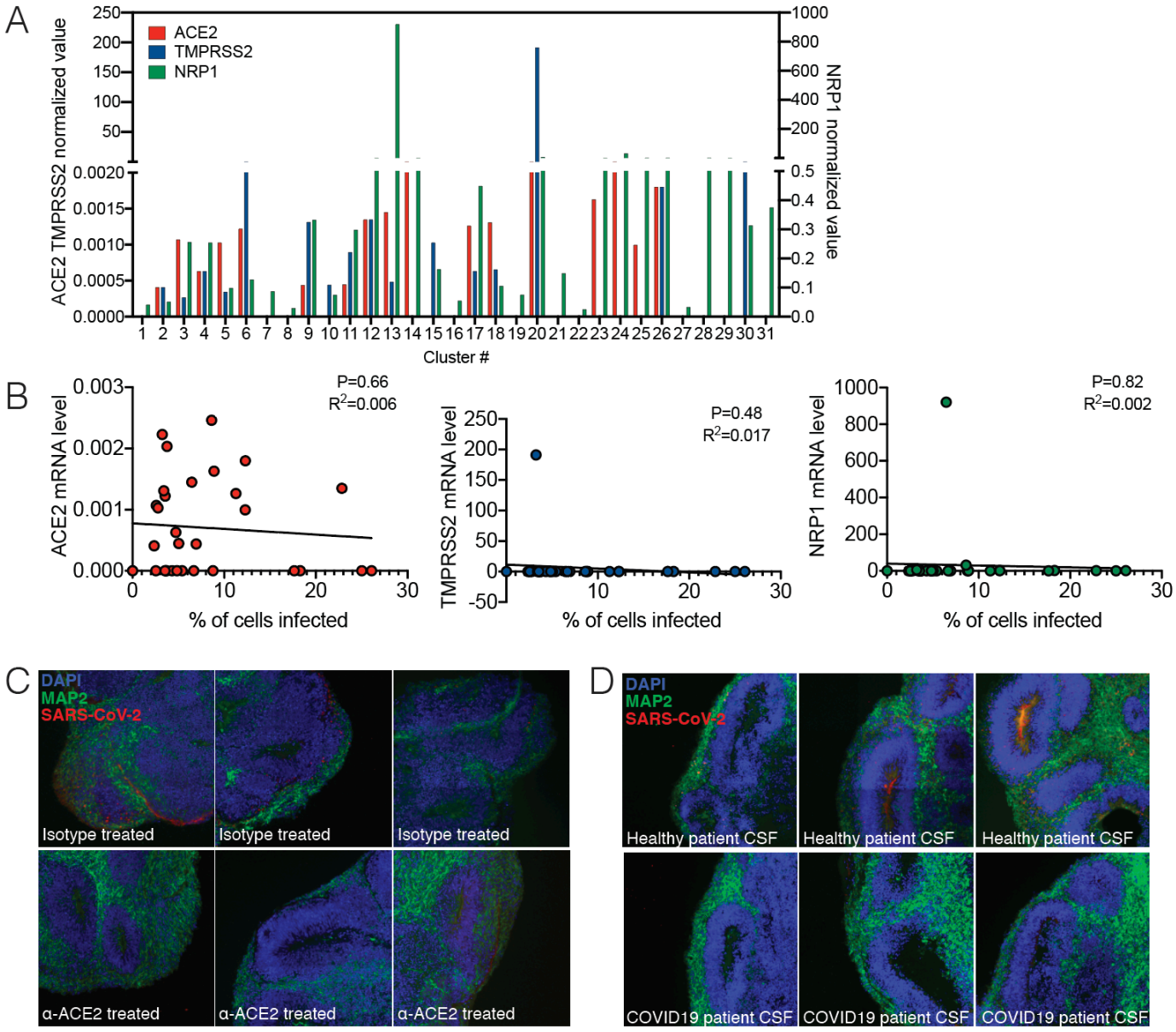

fig. S6: SARS-CoV-2 infection depends on hACE2. (**A**) Expression levels of ACE2, TMPRSS2, and NRP1 from single cell RNA-seq data. (**B**) Correlation of ACE2, TMPRSS2 and NRP1 expression to % of cells infected in each cluster. (**C**) Uncropped images of ACE2-antibody treated organoids shown in 3B. (**D**) Uncropped images of CSF-treated organoids shown in 3E. All experiments were performed with unique organoid n of 4 per condition, with images from n = 12 cortical regions with two IPSC lines.